Research Article | Vol. 25, No. 23 | 13 Nov 2017 | OPTICS EXPRESS 28697
Optics EXPRESS

Performance characteristics of 4-port in-plane and out-of-plane in-line metasurface polarimeters

MICHAEL JUHL,[1,2] CARLOS MENDOZA,[1] J. P. BALTHASAR MUELLER,[3] FEDERICO CAPASSO,[3] AND KRISTJAN LEOSSON[1,2,*]

[1]*Innovation Center Iceland, 112 Reykjavík, Iceland*
[2]*University of Iceland, 101 Reykjavík, Iceland*
[3]*Harvard John A. Paulson School of Engineering and Applied Sciences, Harvard University, Cambridge, Massachusetts 02138, USA*
**kristjan.leosson@nmi.is*

Abstract: In-line polarimeters perform nonterminating measurements of the polarization state of light by sampling only a small part of the total light intensity. In-line polarimeters are used in applications such as polarization state generators and in optical communications. Current polarimeters use multiple optical components in sequence for polarization analysis and therefore often become bulky and expensive. Here, we experimentally demonstrate the operation of compact fiber-coupled polarimeters with high sampling rates, operating at telecom wavelengths, each polarimeter comprising a single ultra-thin metasurface aligned to four photodetectors. We compare two configurations of such metasurface polarimeters, with in-plane and out-of-plane detection, respectively. The metasurface polarimeters reported here show excellent agreement with commercial polarimeters and cover a bandwidth of at least 100 nm.

© 2017 Optical Society of America

OCIS codes: (050.6624) Subwavelength structures; (120.5410) Polarimetry; (220.4241) Nanostructure fabrication; (230.0230) Optical devices; (260.5430) Polarization.

References and links

1. R. M. A. Azzam and N. M. Bashara, *Ellipsometry and Polarized Light* (North-Holland, 1977).
2. C. R. Menyuk and A. Galtarossa, *Polarization Mode Dispersion* (Springer, 2005).
3. J. R. Schott, *Fundamentals of Polarimetric Remote Sensing* (SPIE, 2009).
4. A. Hayat, J. P. B. Mueller, and F. Capasso, "Lateral chirality-sorting optical forces," Proc. Natl. Acad. Sci. U.S.A. **112**(43), 13190–13194 (2015).
5. A. Pierangelo, A. Benali, M. R. Antonelli, T. Novikova, P. Validire, B. Gayet, and A. De Martino, "Ex-vivo characterization of human colon cancer by Mueller polarimetric imaging," Opt. Express **19**(2), 1582–1593 (2011).
6. K. M. Twietmeyer, R. A. Chipman, A. E. Elsner, Y. Zhao, and D. VanNasdale, "Mueller matrix retinal imager with optimized polarization conditions," Opt. Express **16**(26), 21339–21354 (2008).
7. R. M. A. Azzam, "Photopolarimetric measurement of the Mueller matrix by Fourier analysis of a single detected signal," Opt. Lett. **2**(6), 148–150 (1978).
8. D. H. Goldstein, "Mueller matrix dual-rotating retarder polarimeter," Appl. Opt. **31**(31), 6676–6683 (1992).
9. A. Peinado, A. Lizana, J. Vidal, C. Iemmi, and J. Campos, "Optimization and performance criteria of a Stokes polarimeter based on two variable retarders," Opt. Express **18**(10), 9815–9830 (2010).
10. G. E. Jellison and F. A. Modine, "Two-modulator generalized ellipsometry: experiment and calibration," Appl. Opt. **36**(31), 8184–8189 (1997).
11. R. M. A. Azzam, "Division-of-amplitude photopolarimeter (DOAP) for the simultaneous measurement of all four stokes parameters of light," Opt. Acta (Lond.) **29**(5), 685–689 (1982).
12. R. M. A. Azzam, I. M. Elminyawi, and A. M. El-Saba, "General analysis and optimization of the four-detector photopolarimeter," J. Opt. Soc. Am. A **5**(5), 681–689 (1988).
13. R. M. A. Azzam, "In-line light-saving photopolarimeter and its fiber-optic analog," Opt. Lett. **12**(8), 558–560 (1987).
14. P. S. Westbrook, T. A. Strasser, and T. Erdogan, "In-line polarimeter using blazed fiber gratings," IEEE Photonics Technol. Lett. **12**(10), 1352–1354 (2000).
15. N. Yu and F. Capasso, "Flat optics with designer metasurfaces," Nat. Mater. **13**(2), 139–150 (2014).

#303696 https://doi.org/10.1364/OE.25.028697
Journal © 2017 Received 2 Aug 2017; revised 18 Oct 2017; accepted 30 Oct 2017; published 3 Nov 2017

Optics EXPRESS

16. D. R. Smith, W. J. Padilla, D. C. Vier, S. C. Nemat-Nasser, and S. Schultz, "Composite medium with simultaneously negative permeability and permittivity," Phys. Rev. Lett. **84**(18), 4184–4187 (2000).
17. H. Galinski, G. Favraud, H. Dong, J. S. T. Gongora, F. Favaro, M. Döbeli, R. Spolenak, A. Fratalocchi, and F. Capasso, "Scalable, ultra-resistant structural colors based on network metamaterials," Light Sci. Appl. **6**, 16233 (2016).
18. N. Yu and F. Capasso, "Optical metasurfaces and prospect of their applications including fiber optics," J. Lightwave Technol. **33**(12), 2344–2358 (2015).
19. M. Khorasaninejad, W. T. Chen, R. C. Devlin, J. Oh, A. Y. Zhu, and F. Capasso, "Metalenses at visible wavelengths: diffraction-limited focusing and subwavelength resolution imaging," Science **352**(6290), 1190–1194 (2016).
20. J. P. B. Mueller, K. Leosson, and F. Capasso, "Ultracompact metasurface in-line polarimeter," Optica **3**(1), 42–47 (2016).
21. R. A. Chipman, *Handbook of Optics* (MGraw-Hill, 1995), Chap. 22.
22. B. Boulbry, J. C. Ramella-Roman, and T. A. Germer, "Improved method for calibrating a Stokes polarimeter," Appl. Opt. **46**(35), 8533–8541 (2007).
23. J. Lin, J. P. B. Mueller, Q. Wang, G. Yuan, N. Antoniou, X. C. Yuan, and F. Capasso, "Polarization-controlled tunable directional coupling of surface plasmon polaritons," Science **340**(6130), 331–334 (2013).
24. M. Skolnik, *Radar Handbook* (McGraw-Hill, 1970).
25. J. N. Sahalos, *Orthogonal Methods for Array Synthesis: Theory and the ORAMA Computer Tool* (John Wiley & Sons, 2006).
26. J. P. B. Mueller, K. Leosson, and F. Capasso, "Polarization-selective coupling to long-range surface plasmon polariton waveguides," Nano Lett. **14**(10), 5524–5527 (2014).

1. Introduction

Polarization is a property of light that describes the vectorial nature of its electric field oscillations. Stokes polarimeters are devices that measure the four Stokes parameters describing the state and degree of polarization of a light beam. The polarimetric information is crucial in a large number of applications. In materials characterization the measurement of polarization is used, e.g., to determine film thickness and refractive index [1]; in telecommunication it is used to monitor effects such as polarization-mode dispersion, polarization-dependent loss, and polarization dependent properties of optical devices [2]; in remote sensing the polarization information allows to distinguish between surfaces of different structures, remove clutter and image through dust and clouds [3]; in chemistry and biotechnology, polarization is used to measure the concentration and/or purity of optically active substances (such as sugars and antibiotics) using angle of rotation or evanescent chiral sensing [4], or to detect cancer or glaucoma in the human eye [5,6], to name a few examples. Due to the 4-dimensional nature of the Stokes vector, a complete Stokes polarimeter performs at least four intensity measurements. This can be realized in a number of different ways. One of the most common methods is the time-sequential approach, where measurements are separated over time, generally employing a single detector. Such polarization analysis can be carried out using mechanically rotating [7,8] or oscillating waveplates [9], or photoelastic modulators [10]. Products based on all three different approaches are available on the market. None of these configurations are signal-saving and, since the measurement is spread over time, such devices have a limited sampling rate. Another method is division-of-amplitude, where the beam is split up and measured simultaneously using several detectors, e.g. by employing a sequence of beamsplitters and waveplates [11,12]. Signal saving polarimeter designs using the division-of-amplitude method can be realized by employing polarization state analyzers that use only a small fraction of the incident light intensity to measure its polarization [13]. A modern-day example of this configuration is the in-line fiber polarimeter, where two or more polarization-dependent tilted fiber Bragg gratings, separated by a fiber quarter-wave plate, split off a small proportion of the transmitted optical power to four photodetectors [14]. The in-line fiber polarimeter offers a higher sampling rate than the time-sequential method. Some of the measurement accuracy is sacrificed by only measuring a fraction of the signal intensity. However, the accuracy of most commercial in-line fiber polarimeters still lies in the same range as their signal-terminating counterparts. Due to cost, speed or space limitations, the abovementioned solutions are inappropriate for many

Optics EXPRESS

applications such as parallel monitoring of polarization of a large number of channels in optical networks. Furthermore, none of the in-line polarimeters preserves the polarization of the incident light.

Metasurfaces are two-dimensional optical nano-structures that enable the tailoring of the amplitude, phase or polarization of light using dense arrays of sub-wavelength scale optical antennas [15]. In addition to displaying interesting optical phenomena, such as negative refraction and near-zero permittivity or permeability [16,17], metasurfaces also provide a promising platform for simplifying and miniaturizing existing optical components [15,18,19]. In 2016, we presented the concept of a metasurface-based in-line polarimeter [20]. Using a laboratory setup, we demonstrated that all four polarization state analyzers of a Stokes polarimeter could be combined in a single-layered array of sub-wavelength nanoantennas. The ultra-compact design of the metasurface polarimeter, combined with its non-destructive, polarization-preserving features, allows for applications such as feedback-driven polarization generation and large-scale online polarization monitoring in optical communication. In addition to the ultra-compact design that allows for planar integration, the benefits of the metasurface polarimeter include a detection-limited response time, simple and versatile design that can be tailored for operation across a wide range of wavelengths simply by changing the dimensions of the metasurface structure, increased robustness and reduced costs due to the replacement of moving parts and optical components like waveplates with structures produced by conventional lithographic process technology. In the present paper, we provide analysis and comparison of two configurations of packaged fiber-coupled polarimeter devices based on the metasurface principle.

2. Polarimeter design

The four-port metasurface polarimeter is described using the mathematical formalism of the polarimetric measurement and analysis of a standard Stokes polarimeter, see [12,20], where the four power measurements and the incident polarization are related by the *analyzer matrix*

$$\mathbf{P} = \mathbf{MS} \tag{1}$$

where **P** is the measured power from each of the output channels and **M** is a 4x4 matrix with each row containing an *analyzer vector* that characterizes one polarization analyzer [21]. **S** is the Stokes vector of the incoming light given by

$$\mathbf{S} = \begin{pmatrix} S_0 \\ S_1 \\ S_2 \\ S_3 \end{pmatrix} = \begin{pmatrix} I \\ pIs_1 \\ pIs_2 \\ pIs_3 \end{pmatrix} \tag{2}$$

where I is the incident light intensity, p is the degree of polarization (DOP), and s_1-s_3 is the state of polarization (SOP) represented as a point on the surface of the Poincaré sphere.

Calibration of the polarimeter devices was carried out by determining the analyzer matrix from a set of (usually 80) individual reference measurements, using the method described in [22].

The metasurface described in this section consists of arrays of metallic nanorods. A graphical representation of the metasurface design is seen in Fig. 1(a).

Optics EXPRESS

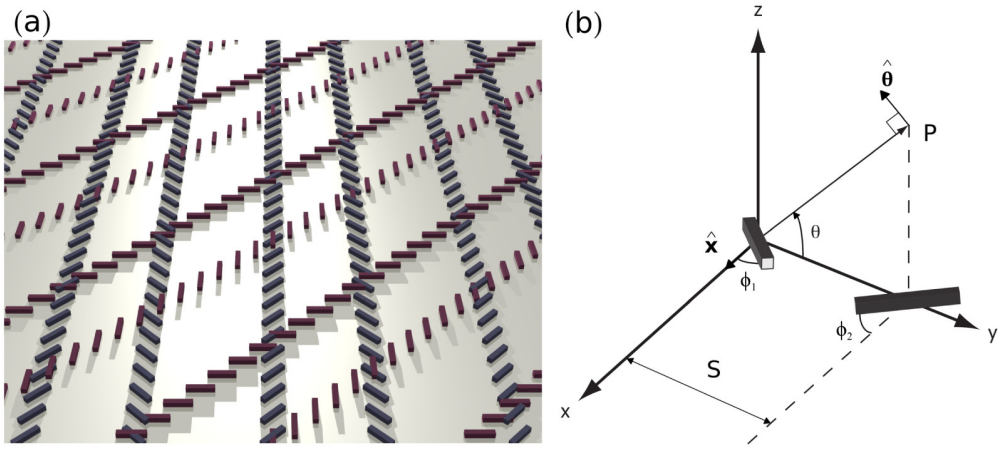

Fig. 1. (a) Graphical representation of the metasurface design. The metasurface consists of columns of sub-wavelength spaced nano-antennas. The antennas in each column are rotated 90° relative to the antennas in the neighboring column. The distance between every second column is twice the resonance wavelength, $2\lambda_0$, and the distance between two column-pairs is $\lambda_0(1 + 1/8)$. The red antenna columns are arranged in a pattern identical to the blue design except from a 45° rotation relative to the blue antenna columns. The height of the antennas are 2 times larger than their designed proportions for visual purposes. (b) Geometry of a phased array with two elements with individual orientation (ϕ_1 and ϕ_2) in the xy-plane. The point of observation (P) is established by the angle θ. One antenna (n = 1) is placed in origo and the other antenna (n = 2) is positioned at (0, S, 0). The direction of the unit vectors in Eq. (3) is shown on the figure. Incident light is parallel to the z-axis.

A metallic nanorod can be modelled as a thin optical dipole antenna. Consider electromagnetic radiation that has a wavelength corresponding to the resonance wavelength of the nanoantennas and is normally incident on the antenna. The antenna then emits radiation as long as the incoming light contains a component of polarization along the long axis of the rod. The far-field radiation pattern of a nanoantenna with length less than a wavelength can be modelled reasonably well as a short dipole. If identical antennas are placed in a subwavelength-spaced 1-dimensional array, the azimuthal radiation pattern is constant along the array. Two parallel columns having antennas rotated ± 45° from their column axis in a fishbone pattern will scatter most efficiently two orthogonal linear polarization components of an incident electromagnetic field [23]. Therefore, the antennas will emit an interference pattern similar to the radiation pattern of a phased array with two elements. The interference pattern depends on the polarization of the incoming wave and the distance between the two columns. The distance between the two columns can be tuned to fit the phase difference between the two orthogonal components of a preferred incoming polarization to obtain a maximum of scattered field intensity in the directions of interest for that particular (generally elliptical) polarization state. The array factor of a two-pair column is given by [20,24,25]

$$\mathbf{A} = \Phi_1 I_1 + \Phi_2 I_2 = \left[\cos(\phi_1)\hat{\mathbf{x}} - \sin(\phi_1)\sin(\theta)\hat{\boldsymbol{\theta}}\right]\cos(\psi) + \left[\cos(\phi_2)\hat{\mathbf{x}} - \sin(\phi_2)\sin(\theta)\hat{\boldsymbol{\theta}}\right]\sin(\psi)e^{i(\delta - kS\cos(\theta))} \tag{3}$$

where

$$I_1 = \cos(\psi), I_2 = \sin(\psi)e^{i\delta}$$

are the excitation currents for each antenna and

$$\Phi_n = \left[\cos(\phi_n)\hat{\mathbf{x}} - \sin(\phi_n)\sin(\theta)\hat{\boldsymbol{\theta}}\right]e^{-i(n-1)kS\cos(\theta)}$$

Optics EXPRESS

is a vector that describes the radiation as a function of the spatial orientation of the n^{th} dipole for n = 1, 2. ψ and δ describe the polarization of the incoming light using the Jones vector model of polarization in complex number representation. ψ is related to the amplitudes $\psi = \arctan(E_y/E_x)$ and δ is the relative phase difference. $k = 2\pi/\lambda$ is the angular wavenumber of the incoming wave. The position of the first dipole (n = 1) is in origo. S is the distance between columns and the azimuthal angle θ is the angle in the yz-plane between y-axis in the sample plane and the axis from origo to the point of measurement P. The x-axis is parallel to the column axes and ϕ_n is the rotation of the n^{th} dipole away from the x axis in the xy-plane normal to the incident light. $\hat{\mathbf{x}}$ is a unit vector parallel to the x-axis, and $\hat{\boldsymbol{\theta}}$ is a unit vector in the angular tangential direction associated to the rotation of θ. The choice of excitation current restricts the dipoles to be perpendicular to each other, i.e. $|\phi_2 - \phi_1| = 90°$. A sketch of the geometry of an individually rotated two-element array is shown in Fig. 1(b) and radiation patterns for 4 different input polarizations are shown in Fig. 2, with $S = \lambda_0(1 + 1/8)$ and $\phi_n = \pm 45°$. λ_0 is the resonance wavelength of the dipole antennas.

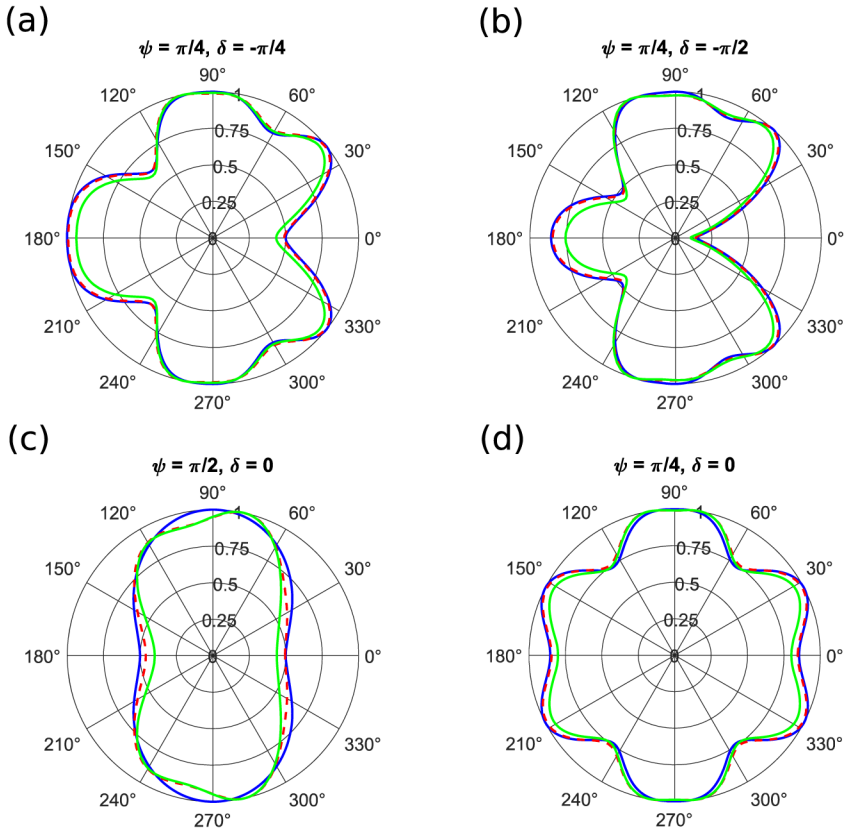

Fig. 2. Radiation patterns of two nanoantennas oriented perpendicularly to each other (± 45°) for different polarizations of the incoming light. The blue line is $|A|^2$ vs θ in the yz-plane (see Fig. 1(b)) normalized to unity using the analytical model Eq. (3), the red dashed line corrects the analytical model for mutual coupling and the green line is $|E|^2$ vs θ normalized to unity using a finite-difference time-domain (FDTD) simulation. (a) is elliptically polarized light with (ψ, δ) = (π/4, -π/4), (b) is circularly polarized light, (c) is linearly polarized light at 45°, and (d) is vertically polarized light.

The inter-antenna distance $S = \lambda_0(1 + 1/8)$ is designed to maximize the array factor Eq. (3) at θ = 0° and θ = 180° (in-plane output) for elliptically polarized light with ψ = π/4 and δ = ± π/4. It is seen that the analytical model fits very well to a finite-difference time-domain

Optics EXPRESS

(FDTD) simulation of two gold antennas with dimensions of 250 nm × 50 nm × 20 nm. Correcting the analytical model for mutual coupling improves the fit even further. The radiation pattern is left/right asymmetric for all elliptical/circular polarizations, as a result of the difference in phase between the two linear orthogonal components of the incoming light's polarization state. The polarization for which the measured power of the scattered field in a given direction (proportional to $|\mathbf{A}|^2$) is maximal corresponds to the analyzer vector. At θ = 0° or θ = 180° the second term in Φ_n vanishes and a signal contrast of 100% on each detector is possible. In the case where θ is 60° or 120°, Φ_1 and Φ_2 will no longer be equal and a theoretical polarization-dependent contrast of only 25% of the overall signal is possible.

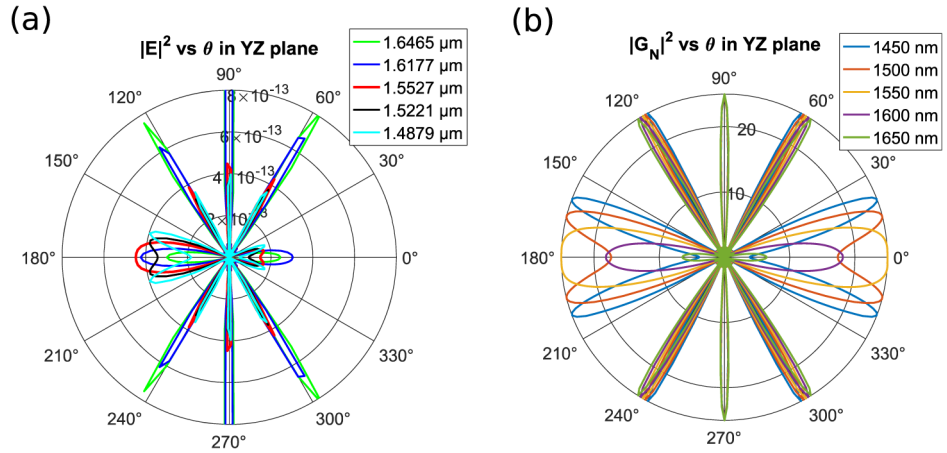

Fig. 3. (a) Wavelength dependence of the finite-difference time-domain (FDTD) simulated radiation pattern, $|E|^2$ versus θ in the yz-plane, of a metasurface consisting of five column-pairs of ± 45°-oriented antennas. Incoming light is elliptically polarized with (ψ, δ) = (π/4, -π/4). (b) Diffraction pattern of a meta-grating with N = 2 and d = $2\lambda_0$ using Eq. (4), $|G_N|^2$ versus θ in the yz-plane, plotted versus different wavelengths. Equation (4) isolates the meta-grating's contribution to the array factor. The plot illustrates that the meta-grating is responsible for the difference in sensitivity to wavelength fluctuations between the in-plane and the out-of-plane design.

Repeating the column-pairs in an array of 2N + 1 elements with a period of d = $2\lambda_0$ will form a meta-grating that covers a larger area and results in a highly directional intensity distribution. To account for the repeated column-pairs the array factor is multiplied with [20]

$$G_N = \sum_{n=-N}^{N} e^{ink\,d\cos(\theta)} \tag{4}$$

In our case, the interesting angles for measurement are the first and second orders of the grating, corresponding to azimuthal angles θ in the yz-plane (see Fig. 1) of 0°, 180° and 60°, 120°, as illustrated in Fig. 3. Figure 3(a) is a plot that shows FDTD simulations of a full metasurface containing five column-pairs and the same S and antenna dimensions as in Fig. 2. Equation (4) is plotted in Fig. 3(b) at different wavelengths and shows the effect of the meta-grating alone.

Optics EXPRESS

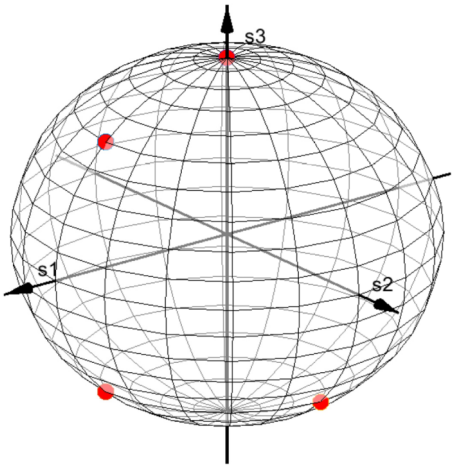

Fig. 4. The four analyzer vectors of a complete Stokes polarimeter depicted on the Poincaré sphere. It is seen that the four polarizations span a volume in SOP space and it is therefore possible to distinguish between the intensity and the DOP.

The four analyzer vectors in the analyzer matrix are defined in a manner analogous to Stokes vectors and they form a basis for the SOP space. If using the four angles of the two grating orders mentioned above the basis will be incomplete and it will not be possible to measure the full SOP. Furthermore, a complete polarimeter that measures the intensity and SOP as well as the DOP needs to have analyzer vectors that span a volume in SOP space [20]. These problems are solved by superimposing another column-pair grating at a 45° angle relative to the first. A distance of $S = \lambda_0(1 + 1/4)$ and an out-of-plane measurement of the first column-pair grating would theoretically result in an analyzer vector with two elliptically polarized states, $(\psi, \delta) = (\pi/4, \pm 3\pi/4)$. Measuring the second column-pair at 0° and 60° would produce an analyzer vector with a circularly polarized state $(\psi, \delta) = (\pi/4, \pi/2)$, and another with an elliptically polarized state $(\psi, \delta) = (\pi/4, -3\pi/4)$, see Fig. 4. However, out-of-plane and in-plane measurement comes with different traits, so here we will focus only on purely in-plane or out-of-plane designs. The in-plane metasurface polarimeter is designed with two 45° superimposed column-pair gratings and distances of $S = \lambda_0(1 + 1/8)$ to obtain (ideally) the best basis for a four-output polarimeter with the constraint that the analyzer vectors consists of two pairs of vectors mirrored about the equator of the Poincaré sphere [12]. Figure 5 shows schematics of a full metasurface, with two superimposed columns-pair gratings, each grating consisting of 5 column-pairs. The arrows illustrate the direction of the incoming light and direction of the scattered light of interest for in-plane and out-of-plane measurements. Figure 5(a) shows the in-plane design and Fig. 5(b) illustrates the out-of-plane design. Theoretically, the analyzer vectors of these two designs do not span a volume in SOP space, but deviations of the analyzer vectors caused by antenna interactions, geometric deviation, internal reflections and/or wavelength dependence are nevertheless large enough to distinguish between changes in DOP and intensity. The in-plane design is well suited for coupling the scattered radiation directly to planar waveguides and could therefore be advantageous in an on-chip polarimeter array design. Furthermore, the signal contrast Eq. (3) and the maximum power to the detector at the designed wavelength (Fig. 3(a)) are larger. The out-of-plane design shows less wavelength dependence, which is mainly an effect of the meta-grating as seen in Fig. 3(b). Furthermore, there are no rescattering or absorption losses in the out-of-plane design, since the scattered field does not propagate along the plane of the metasurface. There is therefore no limit to the overall size of the metasurface, making alignment with the incoming light beam a simpler task.

Optics EXPRESS

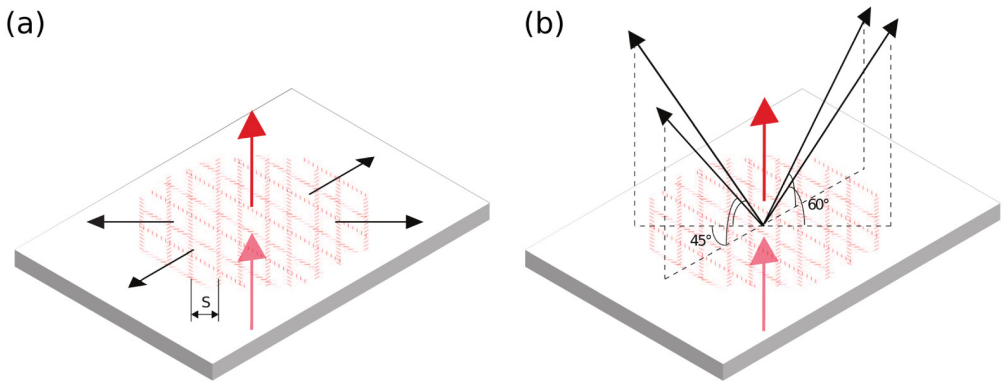

Fig. 5. Schematics of a metasurface polarimeter showing the geometry of the antenna structure placed onto a transparent substrate. (a) The black arrows represent the directions of scattered light, propagating in the plane of the sample surface. (b) The black arrows indicate the angles that can be used for out-of-plane measurements. The scattered field intensity is measured behind the sample (seen from the perspective of the light source). The red arrows illustrate the incident light beam and the light transmitted through the sample.

3. Experiments and results

The arrays of nanoantennas forming the metasurface were fabricated on fused silica substrates. The metasurface structures were patterned using electron beam lithography, gold deposition and lift-off. The resulting nanorods have a thickness of 25 nm, width of approximately 50 nm and a length of 250 nm (approximately 1/4 of a wavelength) and are embedded within a 25 μm layer of dielectric (BCB polymer) for protection. The full metasurface covers an area of 100 μm × 100 μm. Scanning electron micrograph (SEM) images of the metasurface is seen in Fig. 6. In the case of in-plane detection, the substrate was diced such that the substrate edges were perpendicular to the direction of the four scattered light directions. The substrates were fitted into a 3D-printed holder that aligned the sample with four individual TO-canned PIN photodiodes. Another 3D-printed holder was made for the different positions of the detectors in the out-of-plane design. One half of a fiber mating sleeve was used to align a fiber connector to the metasurface, as shown in Fig. 7. This compact polarimeter, consisting of the metasurface chip, a 3D-printed holder, four photodetectors, and one half of a mating sleeve, demonstrates that the polarimeter can be realized without any optical elements between the metasurface and the detectors. This is an important step towards extremely compact polarimeters that integrates detectors on the metasurface chip. A schematic of the setup is seen in Fig. 8. 1510 nm – 1610 nm light from a tunable laser was coupled into a deterministic polarization controller (DPC) and directed to the metasurface. The optical fiber between the DPC and the sample inevitably changes the polarization of the light. Therefore, the polarization of the light transmitted through the sample was additionally measured using a commercial free-space rotating-wave-plate polarimeter. A manual polarization controller was used to ensure that the DPC and the rotating-waveplate polarimeter registered the same polarization state. The output signals from the four detectors on the metasurface polarimeter were fed through an amplification circuit and measured in photoconductive mode. A microcontroller collected a 300-sample set from the four photo-detectors at a rate of 1 kHz. This sampling rate is limited only by the electronics. Approximately 25% of the input power is lost in the metasurface at 1550 nm due to absorption and scattering. A maximum of 0.4% of the total incoming power is scattered to each photodetector.

Optics EXPRESS

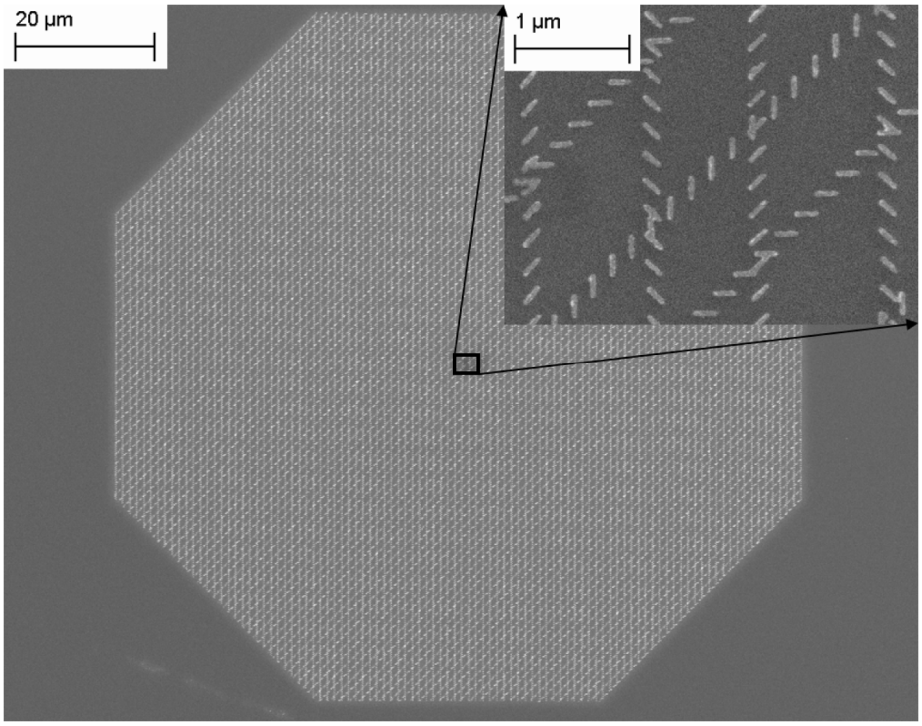

Fig. 6. Scanning electron micrograph (SEM) images of the fabricated metasurface showing the total metasurface structure. Inset: zoom-in of the metasurface displaying the individual antennas of the array.

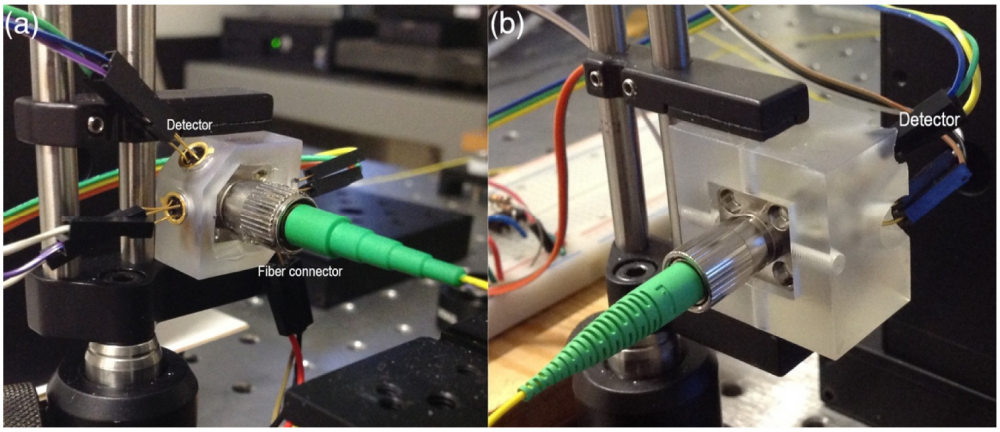

Fig. 7. Images of the in-plane metasurface polarimeter (a) and the out-of-plane polarimeter (b). The incident light enters each device through the optical fiber which is placed in contact with the sample perpendicular to the metasurface. The transmitted light exits through a hole in the back of the 3D holder. Four TO-canned photodiodes are glued into each holder.

Optics EXPRESS

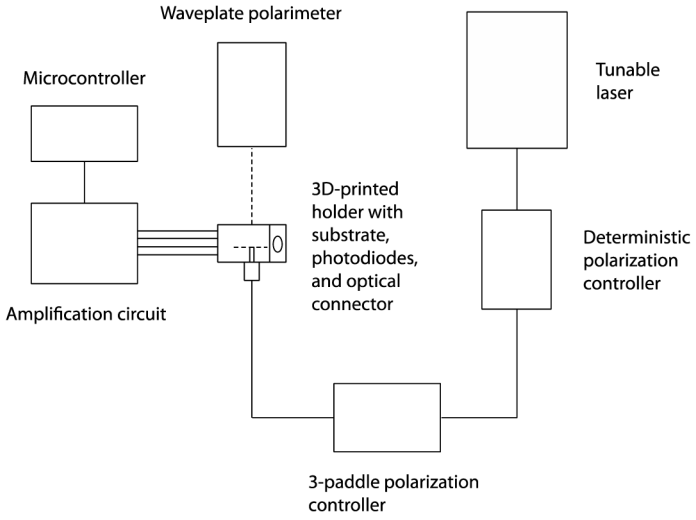

Fig. 8. A sketch of the experimental setup. Light from a tunable fiber laser is coupled through a standard single mode fiber to a deterministic polarization controller. A 3-paddle polarization controller corrects for polarization changes caused by the fiber. The optical connector is placed in contact with the sample by using half of a mating sleeve. A commercial polarimeter is placed behind the sample. Four photodiodes are fitted onto the sample holder and the measured signal is picked up by a microcontroller.

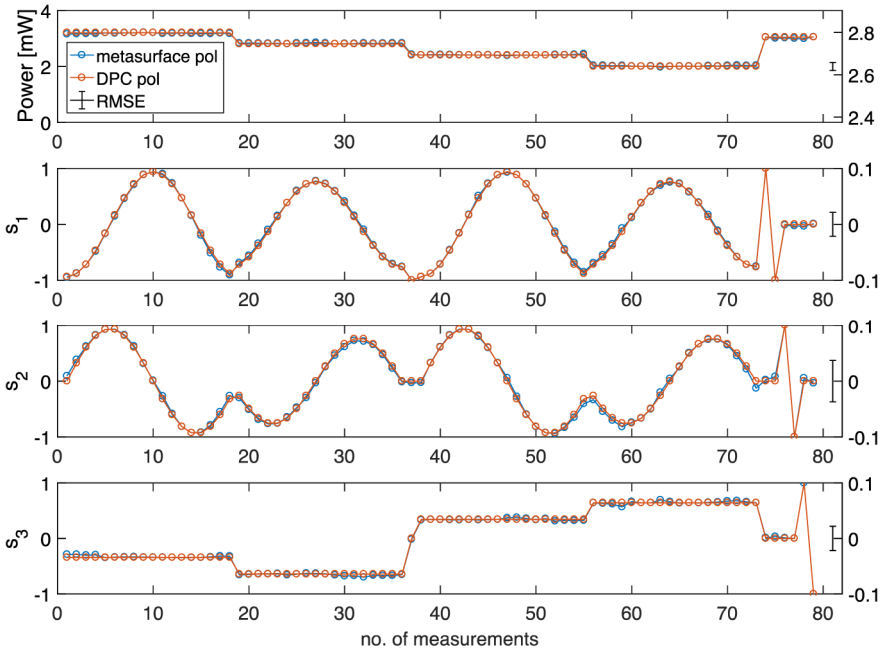

Fig. 9. Polarization measurements at 1550 nm using a device with in-plane design. Each subplot contains one element in the Stokes vector. The first subplot is the power of the incident light, which is proportional to S_0. The next three subplots are the parameters characterizing the state of polarization (SOP), s_1-s_3. The blue dots are the polarization measurements of the metasurface polarimeter, the red dots are the measurements of the deterministic polarization controller (DPC) for comparison. The error bar is the root mean square error (RMSE) giving a measure of the deviation between the two data set, note the 10x change in scale on the y-axes.

Optics EXPRESS

A number of polarization measurements were performed and the results were compared to the polarization state specified by the DPC, using the calibration procedure mentioned in Section 2 [22]. Each metasurface polarimeter was tested at several wavelengths. One set of measurements performed at a wavelength of 1550 nm is shown in Fig. 9 using a device with the in-plane design. Figure 10 shows the root-mean-square-error (RMSE) for both the in-plane and out-of-plane design at several wavelengths. In both cases, a design with antenna column spacing of $\lambda_0(1 + 1/8)$ was used. The device calibration was repeated for each wavelength, since the polarimeter response is substantially wavelength-dependent, as shown in Fig. 3. The same metasurface polarimeter design can therefore be applied across a wide range of wavelengths as long as the spectral information of the incident light source is known *a priori*. As seen in Fig. 11 the wavelength-dependence is quite strong indicating that broadband signals will be affected. Based on these measurements it will be necessary to include wavelength calibration of the polarimeter when wavelength and linewidth is not accurately known. Excellent agreement between the metasurface polarimeter and the DPC is observed. The deviations shown in the figures are not far from the stated accuracy of the state-of-the-art inline polarimeter (IPM5300) from Thorlabs (SOP: ± 0.25° from 1510 nm – 1640 nm). For comparison, Table 1 shows RMSE of the SOP in spherical coordinates for both in-plane and out-of-plane devices.

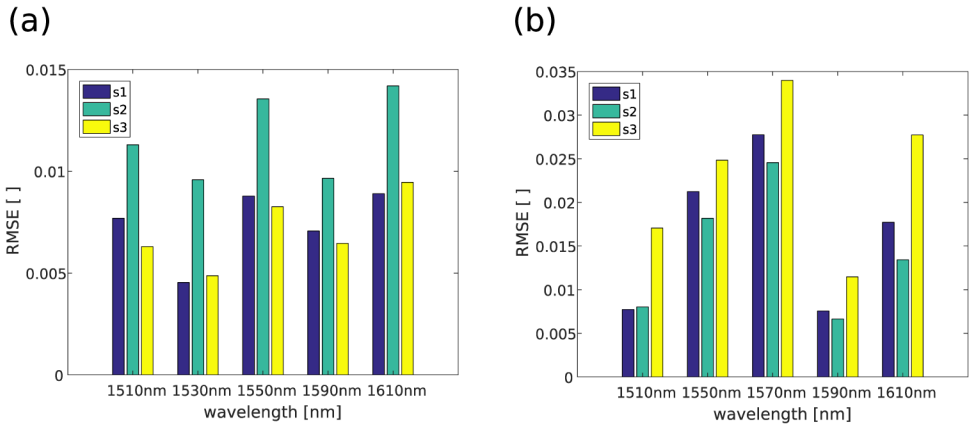

Fig. 10. Root-mean-square-error (RMSE) at wavelengths between 1510 nm and 1610 nm for the in-plane device (a) and the out-of-plane device (b). Each of the columns represents one state of polarization (SOP) parameter.

Table 1. Root-mean-square-error (RMSE) of state of polarization (SOP) parameters

In-Plane device		
λ (nm)	Azimuth error	Ellipticity error
1510	0.44°	0.23°
1550	0.48°	0.29°
1590	0.38°	0.23°
1610	0.54°	0.32°
Out-of-plane device		
1510	0.19°	0.56°
1550	0.81°	0.80°
1590	0.24°	0.39°
1610	0.58°	0.91°

Optics EXPRESS

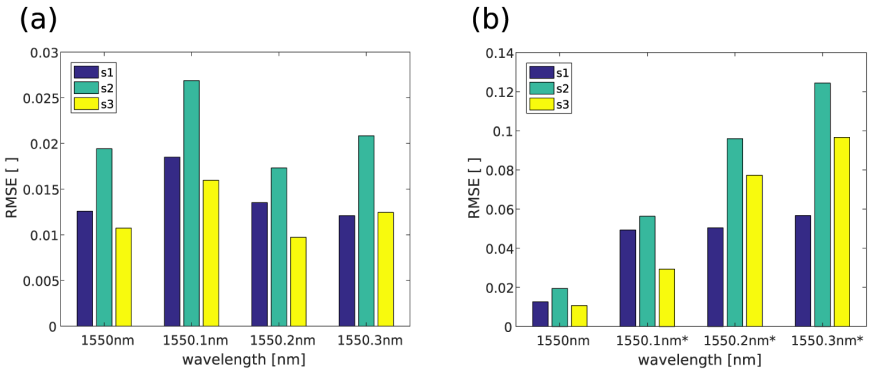

Fig. 11. Root-mean-square-error (RMSE) of each state of polarization (SOP) parameter at wavelengths between 1550.0 nm and 1550.3 nm for the in-plane device. In (a) the data of each wavelength is calibrated individually. (b) shows the same measurements with the difference that the calibration at 1550 nm is used on all four data set (the asterisks indicate the data set that are not calibrated individually).

For the out-of-plane device, about 75% of the scattered light intensity is insensitive to the incoming polarization. Therefore, this configuration is more sensitive to intensity than state of polarization. In other words, the S_0 parameter is more accurate than the s_1-s_3 parameters due to the fact that the intensity element in the analyzer vectors are larger than the SOP elements. Conversely, the in-plane device generally has a lower error on the SOP than the out-of-plane device, because of the better polarization-dependent contrast and the larger power to the detectors. The variation in error between measurements at different wavelengths is mainly caused by wavelength variations of the analyzer vectors.

In [26], the deviation of the analyzer vectors from the theoretically predicted values are very small. The four-output metasurface design, on the other hand, introduces much larger deviations, as seen in Fig. 12. Especially deviations caused by antenna interactions are expected to increase, due to the overlapping of multiple rows of nanoantennas. In order to eliminate this effect, it might be necessary to place two (or more) superimposed metasurfaces in different layers with a vertical spacing larger than the near-field interaction distance. As seen in Fig. 12, the actual analyzer vectors of the in-plane device are very close to each other on the Poincaré sphere. It is clear that a device with a basis for SOP space closer to the theoretically predicted values will yield a lower measurement error. Therefore, it is expected that with future design improvements, the accuracy of the metasurface polarimeter can be made substantially better.

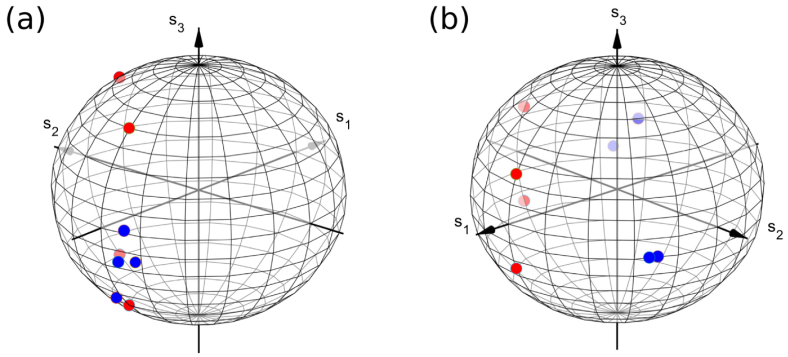

Fig. 12. Analyzer vector position on the Poincaré sphere for a device with (a) in-plane design and (b) out-of-plane design. The analyzer vectors are normalized to unit length. Red dots are the theoretically predicted positions. Blue dots are the measured positions.

Optics EXPRESS

4. Conclusion

We have demonstrated an in-line metasurface polarimeter design that relies on a simple and compact design consisting of only a single polarization-analyzing element and four photodetectors. As there is no need for optical elements between the metasurface and the photodetectors, low-cost fabrication of extremely compact polarimeter devices or device arrays is made possible. The accuracy of the metasurface polarimeter in the current design was shown to be close to commercial in-line polarimeters and further improvement of SOP accuracy is certainly possible, establishing the metasurface polarimeter as a fully viable alternative to existing solutions.

The current polarimeter design was demonstrated to work in the wavelength range 1510 nm – 1610 nm for both the in-plane and the out-of-plane designs. Experiments and simulations suggest that the out-of-plane design has a larger bandwidth. Also, it is better suited for practical applications because a larger metasurface area solves alignment problems without causing additional rescattering and absorption losses. The in-plane design offers a lower error, especially on the SOP.

In summary, our new polarimeter design promises excellent accuracy, compact design, potential for low-cost mass production, and the possibility of modifying the structure (in conjunction with suitable photodetectors) to address a wavelength range well beyond the one presently investigated.

Funding

Icelandic Research Fund (152098051); Air Force Office for Scientific Research (AFOSR) MURI Grant (FA9550-14-1-0389).

128.103.224.178 {ts '2020-05-25 12:56:39'}